

Numerical Study on Thermoelectric Power Generator in Combustor

LI Na¹, WU Peiqin¹, LU Xing², XU Jinhai¹, WANG Qiuwang¹, CHEN Yitung³, MA Ting^{1*}

1. Key Laboratory of Thermo-Fluid Science and Engineering, MOE, Xi'an Jiaotong University, Xi'an 710049, China

2. School of Safety Science and Engineering, Xi'an University of Science and Technology, Xi'an 710054, China

3. Department of Mechanical Engineering, University of Nevada, Las Vegas NV 89154-4027, USA

© Science Press, Institute of Engineering Thermophysics, CAS and Springer-Verlag GmbH Germany, part of Springer Nature 2022

Abstract: Micro gas turbine is a typical distributed energy resource system. The temperature of the burning gas in the combustor reaches 1000 K or even more, which makes a huge temperature difference in the combustor an interesting topic for heat recovery. In this work, thermoelectric devices are used for heat recovery in the combustor of the micro gas turbine. A flow-thermal-electric multiple-physical numerical model is used for the combustor and thermoelectric device power generation system. The effect of the winglet vortex generators installed at the outer wall of the flame tube on the system performance is examined. The numerical results show that the best matching load is about 1.4 times the internal resistance which provides the maximum power output for the thermoelectric generator. Active cascade control of heat transfer enhancement elements on flame tube considering wall safety and conversion efficiency of thermoelectric generator under high temperature and large temperature drop is proposed. The numerical results show that the conversion efficiency of thermoelectric generator can be increased by more than 80%, and the average wall temperature can be reduced by 35 K by using non-uniform arrangement of the winglet vortex generators.

Keywords: distributed energy resources, micro gas turbine, combustor, thermoelectric generator, winglet vortex generator

1. Introduction

Due to the rapid development of the economic society, it is paramount for energy sources to be diverse, flexible and highly efficient. Attention has increased on distributed energy system because of its electrical flexibility and environmental protection [1, 2]. Distributed energy system is also called distributed generation system. There are many kinds of distributed energy resources, such as solar photovoltaic, fuel cells, micro gas turbine (MGT) and batteries [3]. Among these resources, MGT is one of the most advanced

technologies with small friction loss, high precision, and it is suitable for a wide range of temperature [4]. The power of a single MGT ranges from tens to hundreds of kilowatts. Its advantages are compact structure, lightweight, low noise and high reliability [5]. It has important application prospects in defence fields such as aerospace and land. It is rare for a single-cycle MGT to achieve an electrical efficiency of 20% [6]; hence the Brayton cycle with regeneration, which can increase the electrical efficiency of the system, is often adopted [7]. The MGT is composed of three major parts: the compressor, combustor, and turbine. Air is compressed

Nomenclature			
A	heat transfer area/mm ²	w	width of winglet/mm
c_p	specific heat/J·(kg·K) ⁻¹	Greek symbols	
D_h	hydraulic diameter of cold-side channel, mm	α	Seebeck coefficient/V·K ⁻¹
f	friction factor	β	attack angle of winglet/(°)
G_k	generation term	γ	filling factor
H	height of cold-side channel, mm	δ	thickness/mm
h	heat transfer coefficient/W·(m ² ·K) ⁻¹	η	conversion efficiency/%
h'	height of winglet/mm	λ	thermal conductivity/W·(m·K) ⁻¹
I	loop current/A	μ	dynamic viscosity/Pa·s
\mathbf{J}	electrical current density vector/A·m ⁻²	ζ	direction normal to the corresponding wall
k	turbulent kinetic energy/m ² ·s ⁻²	ρ	density/kg·m ⁻³ ; electrical resistivity/Ω·m
L	length of cold-side channel/mm	ε	dissipation rate/m ² ·s ⁻³
l	length of winglet/mm	Subscripts	
\dot{m}	mass flow rate/kg·s ⁻¹	ave	average
Nu	Nusselt number	c	cold side
P	output power/W	cl	ceramic insulation layer
Δp	pressure drop/Pa	cu	copper conductor layer
Q_{in}	heat transfer rate/W	f	fluid
R	internal resistance/Ω	ft	flame tube
Re	Reynolds number	i	sequence label of distance, $i = 1, 2, 3, \dots, 8$
R_{load}	load resistance/Ω	in	inlet
T	temperature/K	max	maximum
ΔT	temperature difference/K	n	N-type TE material
Δt	longitudinal pitch of winglet/mm	oc	open circuit voltage
\mathbf{u}	velocity vector/m·s ⁻¹	out	outlet
V	voltage/V	p	P-type TE material
W	width of cold-side channel/mm	W	winglet

by the compressor and then preheated by the regenerator. The turbine is driven to perform work by the high-temperature and high-pressure gas generated in the combustion chamber and entered in it. In an experiment of an ultra-micro-gas turbine test, the regenerator could improve the thermal efficiency of the system from 14.4% to 28.5%.

Many researchers have devoted their time to the study of improving the efficiency of the MGT system. A common practice is to increase the inlet temperature of the turbine [8]. However, by combining other technologies with the MTG, the system efficiency could have a substantial improvement, as in power plants which are based on the integration between a MGT and combine gasification, anaerobic digestion [9], or a solid oxide fuel cell [10]. Waste heat recovery is also becoming one of the efficient methods to improve the overall performance of the system. The temperature of the burning gas in the flame tube can achieve thousands of the absolute temperature, which makes the huge

temperature difference in the combustor an interesting topic for waste heat recovery. Yazawa et al. [11] theoretically proposed a concept using thermoelectric generators (TEGs) integrated into a 1 kW scale miniature Brayton cycle which could shed new light on questions on the improvement of the performance of the microturbine.

The TEGs which can convert heat into electricity directly, based on the Seebeck effect, have been studied since the 1910s [12]. This technology is an all-solid-state energy conversion technology, without chemical reaction and fluid medium. It has advantages of high reliability, long service life, environmentally-friendliness, etc. It has been widely used for solar thermoelectric devices [13], which is an important technology for solar energy utilization [14], micro combined heat and power system [15], diesel engine system [16], and infrared radiation energy harvesting system [17]. Recently, more efforts have been done on the performance of the analysis of TEGs at the system level. Tian et al. [18] constructed a

mathematic model of segmented TEG and evaluated the relevant factors including operating conditions and geometric parameters on the output performance. The results showed that this segmented TEG was more suitable than the traditional TEG for a high-temperature heat source and for large temperature differences. Meng et al. [19] developed a multiple physical model of thermoelectric conversion system, and the results showed that the non-uniformity of temperature in the flow direction would lead to the deterioration of TEG performance. In addition, the maximum output power would be reduced when too many thermoelectric (TE) modules were placed in the system. Zhou et al. [20] built an analytical model including all thermal resistances to predict the performance of TEG, which was verified by experimental data. By enhancing the heat transfer on the cold side of TEG system, the temperature and thermal resistance on the cold side were greatly reduced, and the output power was obviously improved. Yu et al. [21] examined the TEG with a parallel-plate heat exchanger from low-grade heat resources with simulation. The results showed that the temperature of the fluids in the TEG changed linearly, contrary to the logarithmic change in the general heat exchanger. In the experiment conducted by Niu et al. [22], it was shown that the measured data were consistent with the simulation results, and the hot fluid inlet temperature and flow rate were found to greatly affect the maximum power output and conversion efficiency. A novel TEG integrated recuperator was proposed by Ma et al. [23] using the FLUENT software. Parameter optimisation of the whole system was carried on and results showed that the effect order was: channel width > TE fin thickness > TE fin height. Furthermore, an investigation of the effect of the configuration of winglet vortex generators (WVGs) on the performance of the TEG system was also carried out [24]. It was convinced that by arranging denser elements of heat transfer enhancement at the upstream, the power output performance of the TEG system could be improved without increasing pumping power.

Similar to the low and medium temperature TE power generation systems, the research of high-temperature TE power generation system mainly focuses on improving the output power and energy efficiency. Some theoretical studies have been conducted in combining the TEG with self-powered residential heating systems [15, 25–26]. Despite these efforts, the research done on the combination of the MGT combustor and TEG devices is not much. The temperature difference between the cold and hot fluids of the MGT combustion chamber is huge; hence a strong nonlinear variation of the performance of a TE material with temperature will have a high impact on the performance of the TE device. Furthermore, the driving force of a TE device depends highly on the

temperature difference across the hot side and cold side. The use of a TE device inserted into the combustor to convert the huge temperature difference into electricity will be a good solution for improving the efficiency of MGTs. In this work, a flow-thermal-electric multiple-physical numerical model for the MGT combustor-TE device power generation system is examined by FLUENT software with user-defined function (UDF) codes. To improve the accuracy of the calculation model, the temperature-dependent properties of the TE material are considered in the simulation. Active cascade control of heat transfer enhancement elements on the flame tube considering wall safety and conversion efficiency of TEG under high temperature and large temperature drop condition is proposed. It changes the traditional concept of normal temperature heat transfer in small temperature drop based on uniform thermal resistance. The effect of the enhanced heat transfer elements installed at the outer wall of the flame tube on the system performance is firstly examined. Taking into account the inhomogeneous change in temperature along the wall, the effect of non-uniform arrangement of WVGs on heat transfer and output power performance is studied, offering a new view for integrated approach of MGT-TEG system.

2. Numerical Model and Method

A typical combustion chamber integrated with the TEG in the MGT is shown in Fig. 1, which appears to be cylindrically-shaped. The air from the compressor runs through the annular channel between the flame tube and the outer wall. High-temperature gas enters the turbine. Wang et al. [28] designed and tested a 100 kW MGT combustor prototype by experiment. The combustor was designed using natural gas as its fuel. A single tube structure in which air flowed at a high velocity, in counter-current to cool the wall of the flame tube, was used. Based on this model, this paper explores the integrated design of the combustion chamber and the TE devices by setting the TE elements on the inner wall of the flame tube.

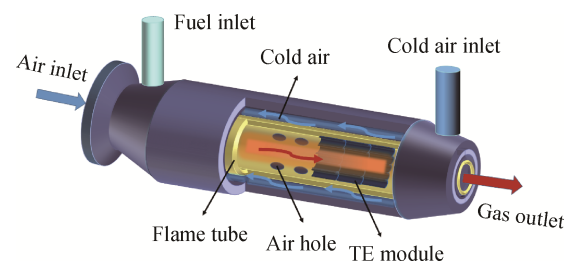


Fig. 1 Physical model of combustor-TE device power generation system

Considering geometric periodicity along the circumferential direction, a periodic element is chosen for the next simulation. This accounts for one-tenth of the whole torus surface. Another modification is that the curvature of the chosen element is very small, so it is rational that the final model simplifies to a three-dimensional (3D) plate. Fig. 2 shows the simplified model of the TEG system. A set of 1×7 TE module sequences is fixed directly into the flame tube, where the hot side of the TE modules is exposed to the high-temperature gas. They are electrically connected in parallel. The countercurrent airflow, which is compressed by the compressor, runs through the channel between the wall of flame tube and combustor, to avoid overheating of the combustor. Besides, the air provides a cold source for the cold side of the TE modules.

The TE module consists of the ceramic insulation layer, copper conductor layer, P-type and N-type TE junctions. The overall dimension of a single TE module is $51.8 \text{ mm} \times 51.8 \text{ mm} \times 4 \text{ mm}$ and the thickness of the ceramic insulation layer (δ_{ci}), copper conductor layer (δ_{cu}) and TE material (δ_{TE}) are 0.9 mm, 0.35 mm and 1.5 mm, respectively. Also, each TE module contains 287 pairs of p-n junctions. The geometry and working conditions of a combustor can be obtained from the literature. On both the hot and cold sides, the channel length (L) is 400 mm; the channel width (W) is 56 mm; the channel height (H) is 15.7 mm and the flame tube thickness (δ_R) is 2 mm. This work aims to establish a numerical prediction model for the combustor-TE device power generation system. Therefore, during the calculation, the inlet flow of the cold channel is assumed to be uniform velocity of 41.17 m/s, and the temperature of inlet air is 873.15 K. The outlet flow is assumed to be fully developed.

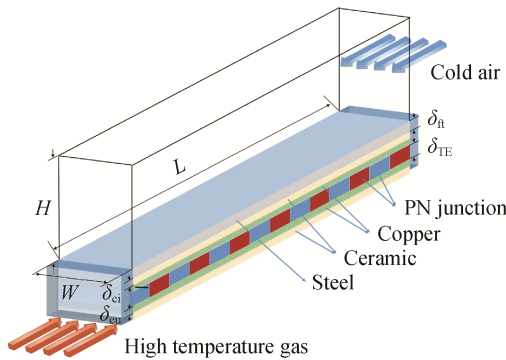


Fig. 2 Simplified model of the TEG system

Based on experimental data from the literature, there is a little difference in the temperature distribution along the inner wall of the flame tube at different positions on the same ring surface. To simplify the physical model, it is assumed that the temperature of the inner wall is only

determined by the axial location, which is indicated in Fig. 3. A specified temperature distribution of the inner wall that has been tested in Ref. [27] is supplied to the hot side of the TE modules.

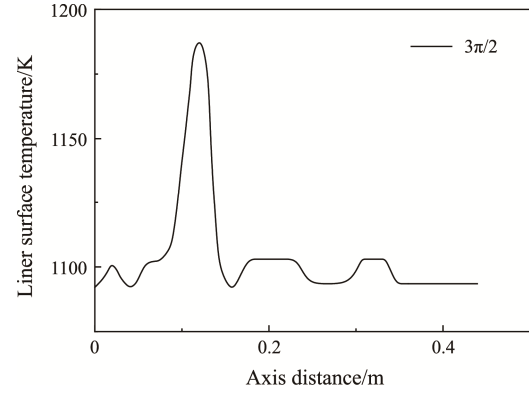


Fig. 3 Temperature distribution on the $3\pi/2$ location of the ring of the combustion chamber surface, reprinted from Ref. [27], copyright 2008, with permission from ASME

The governing equations for the fluid area calculation include continuity equation, momentum equation and energy equation, which are described as:

$$\nabla \cdot \mathbf{u} = 0 \quad (1)$$

$$\rho_f (\mathbf{u} \cdot \nabla \mathbf{u}) = \nabla p + \mu_f \nabla^2 \mathbf{u} \quad (2)$$

$$(\rho_f c_p) (\mathbf{u} \cdot \nabla T) = \nabla \cdot \lambda_f \nabla T \quad (3)$$

where \mathbf{u} is velocity vector; c_p and λ_f are heat capacity and thermal conductivity of the air, respectively.

The Reynolds number of cold air is greater than 9000, so the flow on the cold side is assumed to be a turbulent flow. The standard k - ε turbulent model is adopted in this model. For incompressible fluid flow, the governing equations are expressed as follows:

$$\frac{\partial}{\partial t}(\rho k) + \frac{\partial}{\partial x_i}(\rho k u_i) = \frac{\partial}{\partial x_j} \left[\left(\mu + \frac{\mu_t}{\sigma_k} \right) \frac{\partial k}{\partial x_j} \right] + G_k - \rho \varepsilon \quad (4)$$

$$\begin{aligned} \frac{\partial}{\partial t}(\rho \varepsilon) + \frac{\partial}{\partial x_i}(\rho \varepsilon u_i) = & \frac{\partial}{\partial x_j} \left[\left(\mu + \frac{\mu_t}{\sigma_\varepsilon} \right) \frac{\partial \varepsilon}{\partial x_j} \right] \\ & + \frac{C_{1\varepsilon} \varepsilon}{k} G_k - C_{2\varepsilon} \rho \frac{\varepsilon^2}{k} \end{aligned} \quad (5)$$

where k is the turbulent kinetic energy; ε is the dissipation rate; G_k is the generation term; σ_k and σ_ε are the Prandtl numbers for k and ε , respectively.

Silicon germanium (SiGe) which can withstand high temperature is chosen for the simulation, and the physical properties of SiGe vary with temperature. We list the physical properties of P-type SiGe and N-type SiGe TE materials in Table 1 [28].

Here, T is the Celsius temperature of the TE materials. α_p , α_n , ρ_p , ρ_n , λ_p , λ_n represent the Seebeck coefficient, the

Table 1 Physical properties of TE materials [28]

Physical property	Expression
α_p	$\alpha_p = 10^{-6} \times (559.0770 - 3.2537T' + 1.1269 \times 10^{-2}T'^2 - 1.9552 \times 10^{-5}T'^3 + 1.8826 \times 10^{-8}T'^4 - 9.5888 \times 10^{-12}T'^5 + 2.0179 \times 10^{-15}T'^6)$ 923 K $\leq T' \leq$ 1323 K
α_n	$\alpha_n = (-10^{-6}) \times (526.1755 - 6.5501T' + 2.0189 \times 10^{-2}T'^2 - 3.3191 \times 10^{-5}T'^3 + 3.0903 \times 10^{-8}T'^4 - 1.5074 \times 10^{-11}T'^5 + 2.9338 \times 10^{-15}T'^6)$ 923 K $\leq T' \leq$ 1323 K
ρ_p	$\rho_p = (10^{-5}) \times (3.3350 - 1.6383 \times 10^{-2}T' + 6.4139 \times 10^{-5}T'^2 - 1.3790 \times 10^{-7}T'^3 + 1.7665 \times 10^{-10}T'^4 - 1.2208 \times 10^{-13}T'^5 + 3.4992 \times 10^{-17}T'^6)$ 923 K $\leq T' \leq$ 1323 K
ρ_n	$\rho_n = (-10^{-5}) \times (105.1983 - 0.9603T' + 3.4019 \times 10^{-3}T'^2 - 6.3453 \times 10^{-6}T'^3 + 6.5952 \times 10^{-9}T'^4 - 3.6026 \times 10^{-12}T'^5 + 4.186 \times 10^{-16}T'^6)$ 923 K $\leq T' \leq$ 1323 K
λ_p	$\lambda_p = 46.5529 - 0.3737T' + 1.3481 \times 10^{-3}T'^2 - 2.5249 \times 10^{-6}T'^3 + 2.6010 \times 10^{-9}T'^4 - 1.4043 \times 10^{-12}T'^5 + 3.1202 \times 10^{-16}T'^6$ 923 K $\leq T' \leq$ 1323 K
λ_n	$\lambda_n = 81.4993 - 0.6201T' + 2.0109 \times 10^{-3}T'^2 - 3.3427 \times 10^{-6}T'^3 + 2.9362 \times 10^{-9}T'^4 - 1.2433 \times 10^{-12}T'^5 + 1.8241 \times 10^{-16}T'^6$ 923 K $\leq T' \leq$ 1323 K

electric resistivity and the thermal conductivity of the p-type and n-type TE materials, respectively.

The TE element is governed by current density continuity equation, non-ohmic current-electromotive force constitutive equation and energy equation, which are written as:

$$\nabla \mathbf{J} = 0 \quad (6)$$

$$\nabla V = -\alpha \nabla T - \rho \mathbf{J} \quad (7)$$

$$\nabla (\lambda \nabla T) + \rho \mathbf{J}^2 - T \mathbf{J} \left[\frac{\partial \alpha}{\partial T} \nabla T + (\nabla \alpha)_T \right] = 0 \quad (8)$$

where V represents the electromotive force; \mathbf{J} is the current density vector. In Eq. (8), the second, third, and fourth terms represent the Joule heating, Thomson, and Peltier effects, respectively. The Joule heating, Thomson, and Peltier effects are negligible in the steel domain.

The electrical and thermal boundary conditions for terminal-in at the inlet end of the hot-side TE fins are described as:

$$\mathbf{J} = \frac{I}{A_\xi} = \frac{V_{oc}}{A_\xi (R_{in} + R_{load})}, \text{ and } \frac{\partial T}{\partial \xi} = 0 \quad (9)$$

where ξ donates the direction normal to the corresponding wall.

The terminal-out boundary at the outlet of the TE fin is regarded as the ground voltage:

$$V = 0, \text{ and } \frac{\partial T}{\partial \xi} = 0 \quad (10)$$

The air in the cold-side channel is assumed to be 3D, steady and incompressible. The Reynolds number of working fluids is calculated by:

$$Re = \frac{\rho_f u D_h}{\mu_f} \quad (11)$$

where u is inlet velocity of the cooling air; D_h is the hydraulic diameter of the cold-side channel. ρ_f and μ_f are the density and dynamic viscosity of the air at the inlet temperature, respectively.

When the load resistance in the simulation is given, the output power and input heat transfer rate of the combustor-TE device system are calculated by the expressions as follows:

$$P = I^2 R_{load} \quad (12)$$

$$Q_{in} = \dot{m} c_p (T_{out,c} - T_{in,c}) \quad (13)$$

where I and R_{load} represent the current and load resistance of the system, respectively. c_p represents the specific heat capacity of cold fluid. $T_{out,c}$ represents outlet temperature of cold fluid and $T_{in,c}$ represents inlet temperature of cold fluid.

Eqs. (6)–(8) and (12)–(13) together with temperature-depended physical properties of TE materials shown in Table 1 are written in UDF codes which are subsequently compiled and operated in FLUENT. Detailed description of numerical computing method can be seen in our previous work [23]. Then in each iteration, UDF calculates the output power according to the temperature distribution of TEG module. The thermal conversion efficiency (η) of the TE modules is defined as:

$$\eta = \frac{P}{Q_{in}} \times 100\% \quad (14)$$

The flow-thermal-electric multiple-physical numerical model is examined by the FLUENT software for the combustor-TE device power generation system that considers temperature-depended properties of the TE material. Based on structured heat transfer and fluid flow

models in the simulated environment, a UDF code is established to realise the coupling of the liquid-solid model. 3D, double precision separate solvers are used to solve the governing equations mentioned above. The semi-implicit method for pressure linked equation algorithm is used for the pressure-velocity coupling term. Also, the second-order upwind scheme is used for convection and diffusive terms. The convergence criteria for continuity equation, momentum equation, energy equation, current density, Seebeck electromotive voltage and Ohmic electric voltage are 10^{-4} , 10^{-4} , 10^{-4} , 10^{-15} , 10^{-15} and 10^{-10} , respectively.

3. Grid Independence Test and Model Validation

In the whole calculation zone, structured grids are applied in the control domains. To ensure the accuracy of the calculation results, the grid independence test is necessary. Four sets of grid systems with 0.511, 0.825, 1.65 and 2.24 million cells are tested, respectively. Fig. 4 shows that the output power decreases as the grid number increases. There is a similar tendency in the relationship between the efficiency and grid number. The grid system with 1.65 million cells is chosen for the numerical simulation considering the balance between the accuracy and the calculation time.

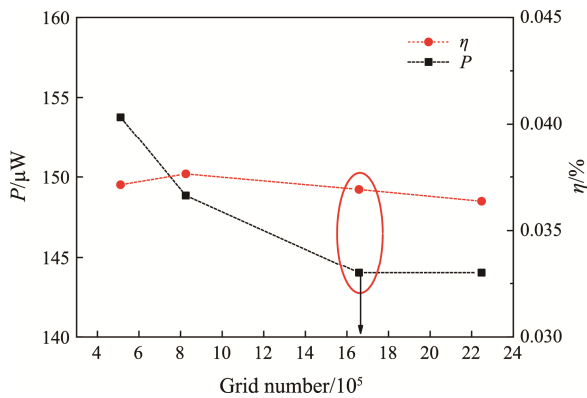
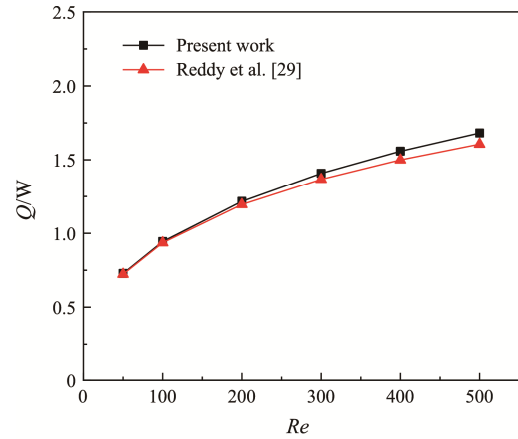


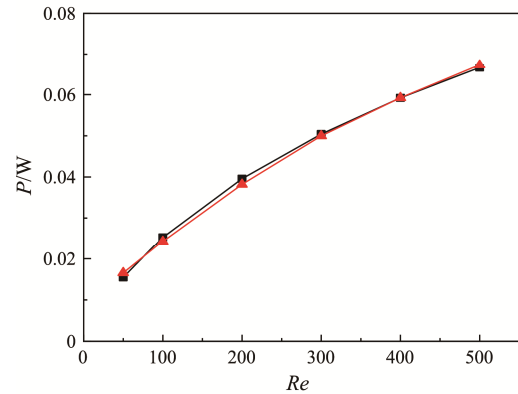
Fig. 4 Grid independence test

The validation of the TE-hydraulic performance is conducted to ensure the accuracy of the numerical method. The results are depicted in Fig. 5(a)–(b). For validation of the TE-hydraulic performance, the simulation results are compared with the work conducted by Reddy et al. [29]. The geometric parameters and boundary conditions of validated model are the same as Reddy's, and assumed that the physical properties of TE materials are changed with temperature. The geometrical dimensions of P- and N-type TE legs, copper connector, copper interconnector and inner flow channel are 5 mm×5 mm×5 mm, 10 mm×5 mm×1.5 mm, 10 mm×10 mm and 1.5 mm×8 mm, respectively. The temperature of cold

side is set as 300 K and 550 K for the inlet temperature of hot side. Fig. 5(a) shows that the maximum deviation of the input heat for the TE module is less than 5%, while Fig. 5(b) shows that the maximum deviation for output power is less than 7%, compared with the results of Reddy et al. [29]. The high matching of our methods and published data indicates the numerical model is accurate.



(a) Validation of input heat



(b) Validation of output power

Fig. 5 Validation of the TE-hydraulic performance

The Nusselt number (Nu) and friction factor (f) are used to validate the fluid flow and heat transfer model, respectively. The schematic of the testing channel is shown in Fig. 6. Nu and f are calculated using Eq. (15) and Eq. (16) based on the computational fluid dynamics results. As shown in Fig. 7, the maximum relative deviation of the Nu is 11.66%, while its average relative deviation is 7.56%. The maximum relative deviation of f is 6.59%, while its average relative deviation is 4.16%. The results of our work agree well with the results calculated by the correlations of Gnielinski and Blasius. Consequently, the numerical method in this work is reliable.

$$Nu = \frac{hD_h}{\lambda_f} \quad (15)$$

$$f = 2 \frac{D_h}{l} \frac{\Delta p}{\rho_f u^2} \quad (16)$$

where Nu and f are calculated by correlations of Gnielinski and Blasius:

$$Nu = \frac{\left(\frac{f_g}{8}\right) (Re - 1000) Pr}{1 + 12.7 \sqrt{\frac{f_g}{8}} (Pr^{2/3} - 1)} \left[1 + \left(\frac{D_h}{l}\right)^{2/3} \right] \left(\frac{T_g}{T_w}\right)^{0.45} \quad (17)$$

$$f = 0.3164 / Re^{0.25} \quad (18)$$

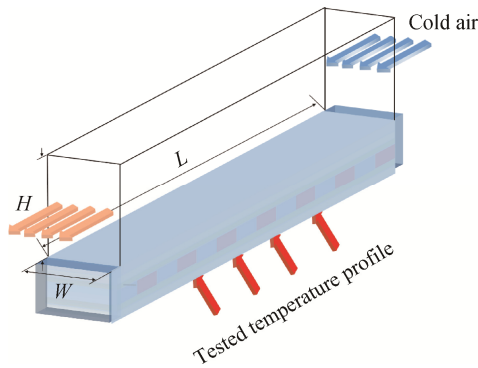
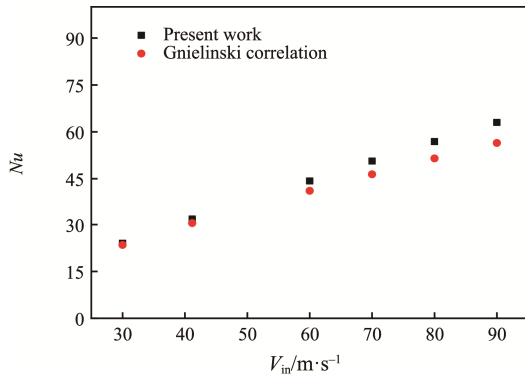
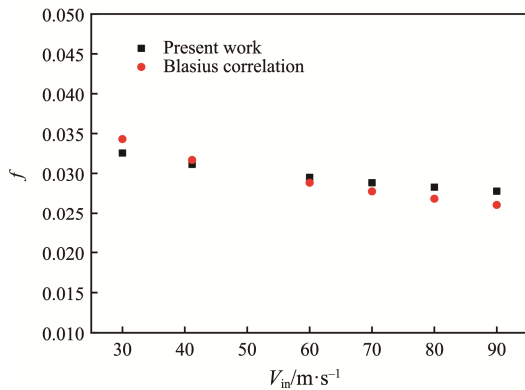


Fig. 6 The testing channel of fluid flow and heat transfer model



(a) Validation of Nusselt number



(b) Validation of friction factor

Fig. 7 Validation of fluid flow and heat transfer model

4. Results and Discussion

4.1 Performance of combined power generation system with smooth cold-side channel

4.1.1 Influence of external load resistance of TEG modules on the performance

When the external load resistance of the device is equal to the internal load resistance, the output power of the device reaches its peak value. This is derived from electrical theory. The optimal ratio of the load resistance to the internal resistance for the TEG system follows quite a different trend [30, 31]. Fig. 8 shows thermoelectromotive force (V), internal resistance (R) and current with an external load resistance of the combined power system for the TEG system with 71 pairs of p-n junctions in each module and the changing trend of the output performance with the external load resistance (R_{load}). It shows that an increase in R_{load} has a minor effect on the voltage and R , which are approximately 5.23 V and 21.29 Ω , respectively. However, the current decreases as R_{load} increases. Fig. 8(c) shows that the changing trend of the power output versus R_{load} follows parabolic curves. When R_{load} is 30 Ω , the maximum output power and efficiency are 0.31 W and 0.9%, respectively. It should be noted that the optimum resistance ratio occurs is greater than one. The portion of the external resistance that is greater than the internal resistance in order to achieve the maximum output power is derived from finite heat sink in the realistic TE device. In the realistic device, the temperature difference across the TE leg is depended on the resistance, which can be expressed by an implicit equation:

$$R_L = R_{in} + \frac{2R_L(R + R_L) \frac{d}{dR_L}(\Delta T)}{\Delta T} \quad (19)$$

The increased current in TE leg makes an innegligible decrease in temperature difference across the leg, which leads to the optimal current lower than the ideal condition ($R_L = R_{in}$). In other words, the optimal external load resistance is larger than that condition. The second term on the right side of the expression reveals effect of realistic heat sink in the practice TE device on output performance. In actual TE devices, the temperature difference across the leg is closely related to the external load resistance, or current in the circuit. This highlights the necessity for a maximum power point tracking (MPPT) device integrated into an energy harvesting circuit for optimum thermoelectric module performance because for a realistic TEG system, the maximum output performance occurs when the external load resistance is not equal to internal resistance. The power described below is the maximum power; i.e. the power when the load resistance is 1.4 times the internal resistance.

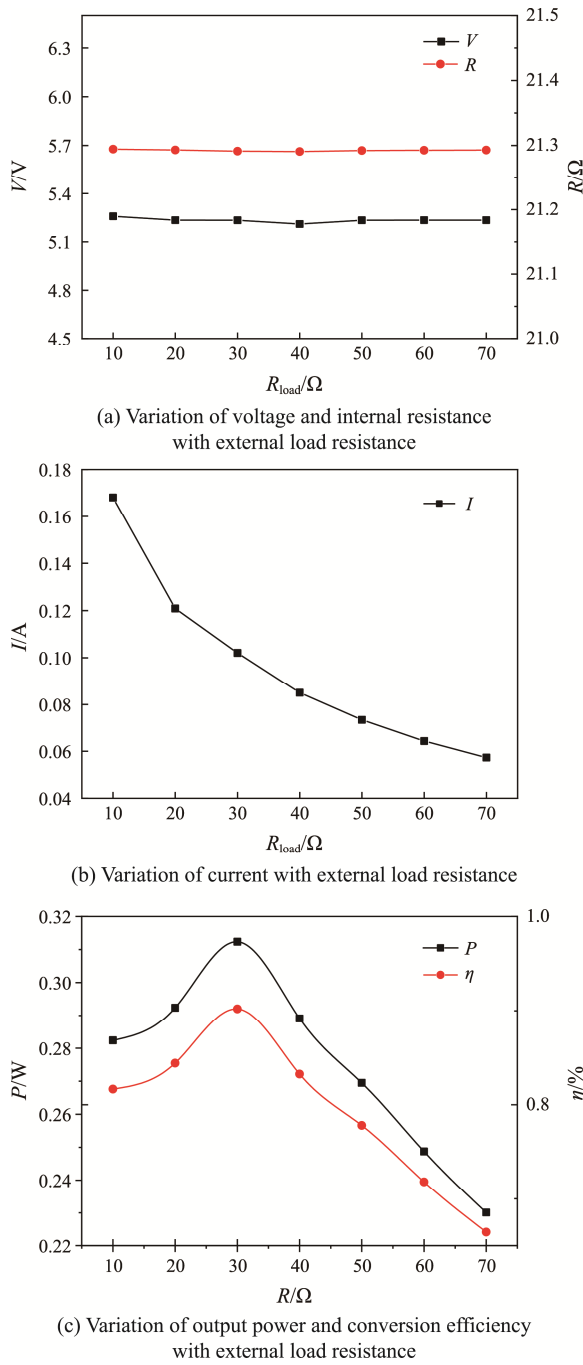


Fig. 8 Effect of external load resistance on the performance of the combined system

4.1.2 Influence of filling factor of TEG modules on the performance

This section examines whether more TE pairs in the TE modules yield better output performance. The filling factor γ is defined as the ratio of the area of the TE pairs to the total area of the wall. For the wall dimensions given above, 287 pairs of P-N junctions could fill up a single TEG module ($\gamma=1$). We select four sets of TE system which have 71 ($\gamma=0.25$), 127 ($\gamma=0.45$), 241 ($\gamma=0.85$) and 287 ($\gamma=1$) TE pairs in each TE modules.

Fig. 9 shows that under the matched load, the output power (P) and the TE conversion efficiency (η) of the system increase at first and then decrease when the number of P-N junctions increases. The maximum P and η are 0.31 W and 0.9%, respectively, at $\gamma=0.25$.

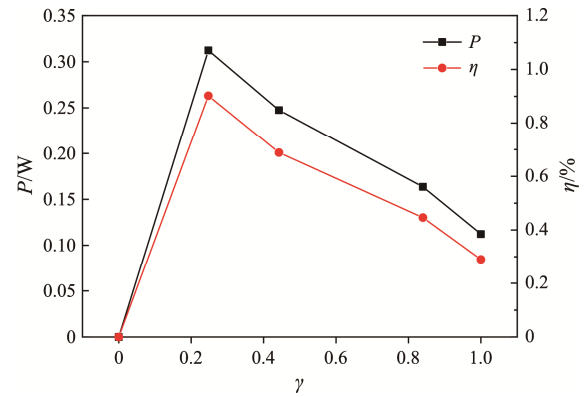


Fig. 9 Variation of output power, conversion efficiency with filling factor

Fig. 10 depicts the changing trend of temperature difference on the hot and cold sides of the TE modules with filling factor. The figure shows that under the given four working conditions, with the increase of γ , the temperature difference decreases, and the maximum ΔT is 42.2 K at M7, where $\gamma=0.25$. Because the Seebeck electromotive force is proportional to ΔT , and a small γ represents a small internal resistance, or equivalently, the optimum filling factor of a typical high-temperature TEG integrated system is below 0.3, and the present model is 0.25. In the optimized case ($\gamma=0.25$), as there are less TE materials, the total thermal resistance between the hot and cold fluids is greater. The hot side temperature almost keeps unchanged under different TE filling factors, while the cold side temperature increases. Therefore, the temperature difference is higher with a greater filling factor. From the results, 71 pairs of P-N junctions ($\gamma=0.25$) are selected for further study, and the matched load resistance is 40 Ω .

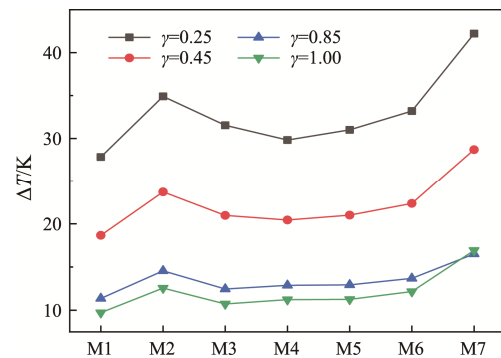


Fig. 10 Variation of temperature difference between the hot and cold side of TE modules with filling factor

4.2. Performance of combined power generation system with enhanced heat transfer elements

Since the temperature of hot side of TEG module is given, the heat transfer enhancement of the cold air channel not only decreases the cold side temperature, but also improves the output voltage owing to the increase of the temperature difference across the TEG module. This can be achieved by adding a set of winglet longitudinal vortex which can enlarge the convective heat transfer area and reduce the thermal resistance from the cold air to the wall; hence the temperature of the wall is decreased. Furthermore, we do a detailed investigation of the influence of the mounting position of the winglet on the output performance. Considering the configuration of the winglet pairs, factors like geometric parameters, number and uniformity contribute equally to the heat transfer and fluid flow performance and have a similar effect on temperature distribution along the flow. Therefore, the number of winglet pairs in the uniform and non-uniform channels with the same structure is nine.

Fig. 11 shows the overall configuration of the cold-side channel. Fig. 11(a) exhibits the winglet pairs with a length (l_w) of 20 mm, width (w_w) of 2 mm and height (h'_w) of 5 mm. The transverse pitch (t_w) is 4 mm and the attack angle (β) is 45° . The temperature field of the fluid flow and solid field can be controlled by adjusting the mounting position of the winglet pairs in the cold-side channel. Fig. 11(b) shows the smooth, uniform and non-uniform channels, respectively. In uniform channel the longitudinal pitch between each pair is 40 mm. For the non-uniform channel, case 1, the winglet pairs in the upstream of airflow are much denser than the downstream; i.e. Δt_1 is kept as 75 mm, while Δt_2 is 55 mm and Δt_3 – Δt_8 are fixed at 30 mm, while case 2 is just the opposite of case 1: Δt_1 – Δt_6 are fixed at 30 mm, while Δt_7 is 55 mm and Δt_8 is 75 mm. In the uniform channel and non-uniform channel of case 1, the distance is 30 mm between the first winglet pair and the entrance and 30 mm between the last winglet and the exit. Table 2 summarises geometric parameters of the cold air channel.

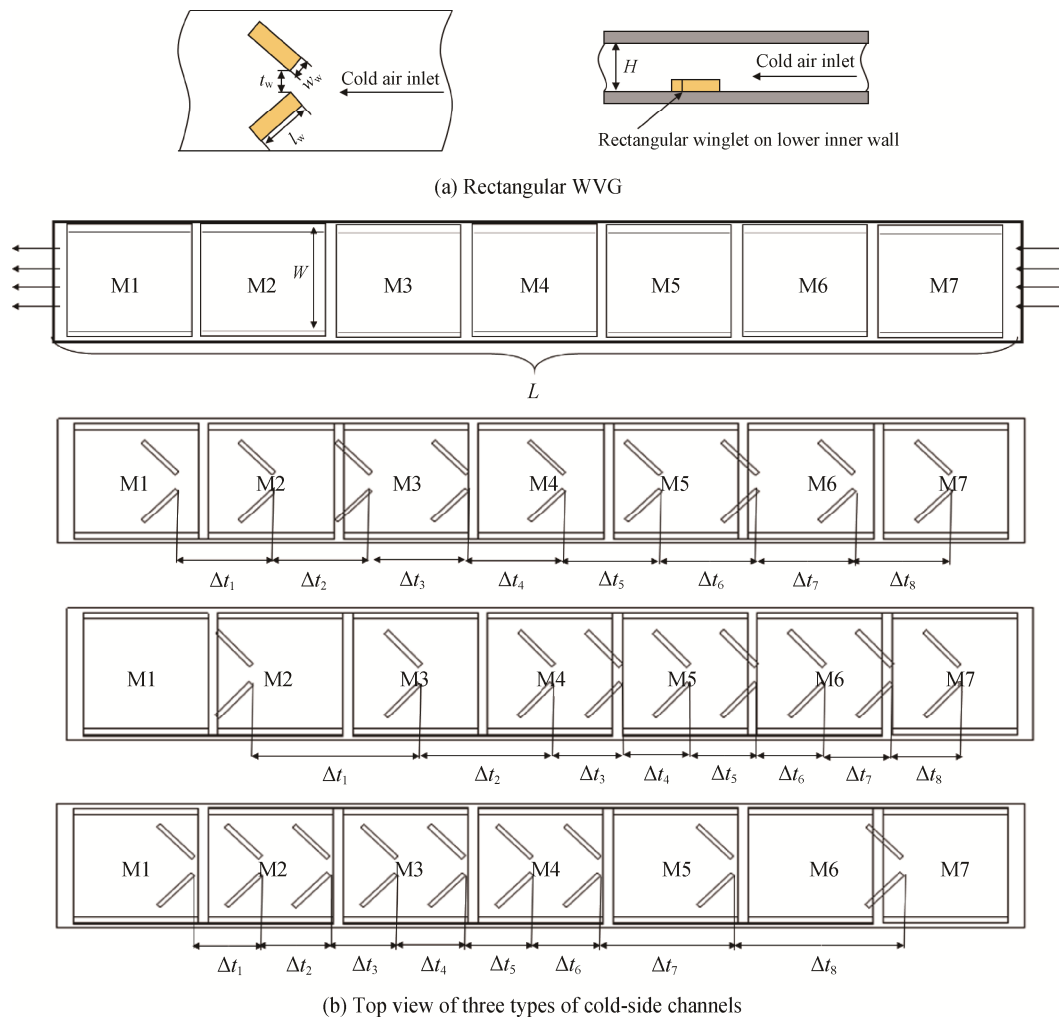


Fig. 11 Configuration of winglet pairs in cold-side channel

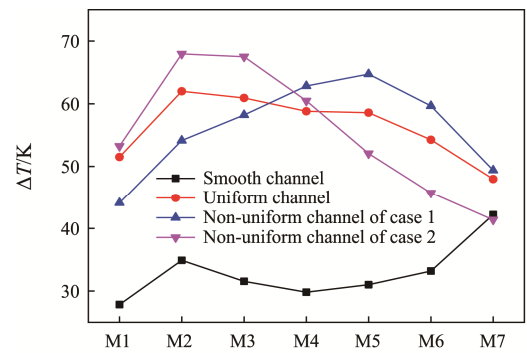
Table 2 Summary of geometric parameters of the cold air channel

Parameter	Unit	Symbol	Value
Length of channel	mm	L	400
Width of channel	mm	W	56
Height of channel	mm	H	15.7
Number of winglet pairs	—	N	9
Length of winglet	mm	l_w	20
Width of winglet	mm	w_w	2
Height of winglet	mm	h_w	5
Transverse pitch of winglet	mm	t_w	4
Attack angle of winglet	°	β	45
Longitudinal pitch of winglet in uniform channel	mm	$\Delta t_i (i=1-8)$	40
Longitudinal pitch of winglet in non-uniform channel (case 1)	mm	$\Delta t_1/\Delta t_2/\Delta t_3 (i=3-8)$	55/75/30
Longitudinal pitch of winglet in non-uniform channel (case 2)	mm	$\Delta t_1 (i=1-6) / \Delta t_7/\Delta t_8$	55/30/75

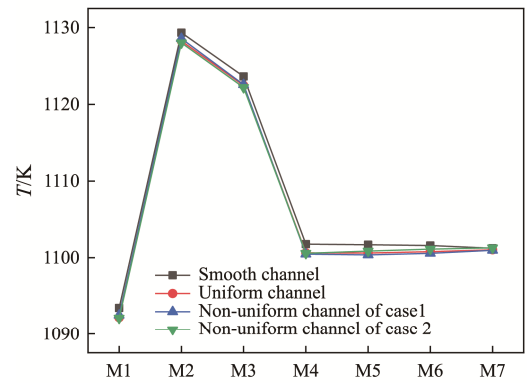
Fig. 12 shows the numerical results of temperature distribution on the hot and cold sides of the TE modules with four sets of cold side channels. Fig. 12(a) shows that in the smooth channel, the maximum temperature difference between the hot and cold ends of the TE module occurs at the tail section (M7) of the combustor where the cold air is minimally influenced, which is about 42 K, while the temperature difference is quite smaller at the head (M1) and middle (M4) sections of the combustor. This is because the temperature of heated air rises while the wall temperature is lower at these locations; hence the difference is quite small. The heat transfer gets improved by mounting winglet pairs. The average temperature difference in the smooth channel is 33 K and increases to 56.3 K, 56.2 K and 55.5 K, respectively in the uniform channel, the non-uniform channel of case 1 and the non-uniform channel of case 2. Fig. 12(b)–(c) shows that the temperature on the hot side is fairly the same as the temperature on the cold side reduces. Thus, the temperature difference increases after enhancing the heat transfer in the cold-side channel. The disturbing effect of the WVG greatly enhances the heat exchange between the cold fluid and the wall, and it can be seen that the temperature difference rises significantly in the places where the WVGs are denser, but for the channels where the WVG are evenly arranged, the temperature difference at each TE module rises to the same extent.

Fig. 13(a)–(b) show the numerical results of the output performance of the TEG system with four sets of cold-side channels. The thermoelectromotive force (V) follows the Seebeck effect which is proportional to the temperature difference on the hot and cold ends of the TEG module. In the smooth channel, the maximum

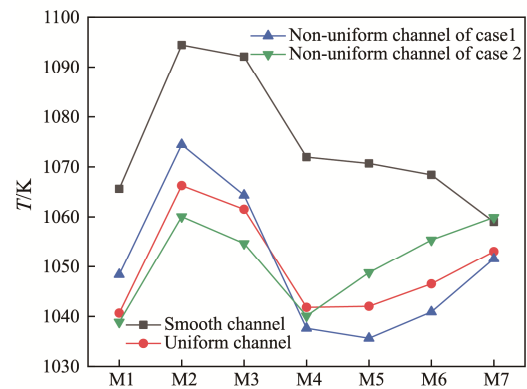
voltage is 0.96 V at M7 while the minimum voltage is 0.63 V at M1 and the average voltage is 0.77 V. Voltage at the uniform channel gets evenly promoted with an average value of 1.29 V. However, for the non-uniform channel, the increment of voltage is larger where the winglet pairs are denser; the average voltage values are 1.29 V and 1.27 V, respectively, for case 1 and case 2. Fig. 13(b) shows the output power with four sets of cold-side channels. After the heat transfer enhancement, the power of the other channel is increased by twice as much as that of the smooth channel. Also, the TE efficiencies are



(a) Temperature difference on the hot and cold sides of TE modules with four sets of cold-side channel



(b) Temperature on the hot side with four sets of cold-side channels



(c) Temperature on the cold side with four sets of cold side channel

Fig. 12 Temperature distribution on the hot and cold sides of TE modules with four sets of cold side channel

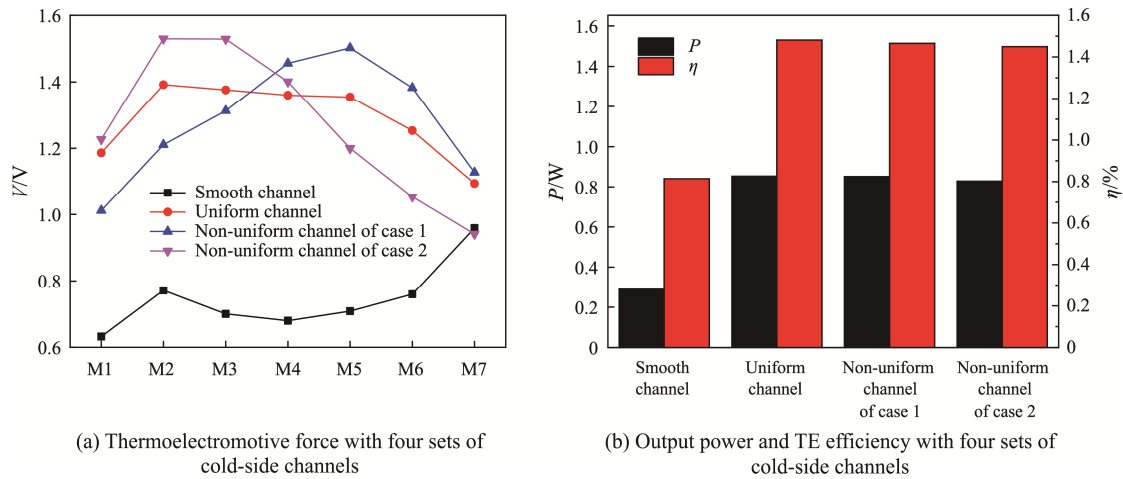


Fig. 13 Output performance of the TEG system with four cold-side channels

Table 3 Wall temperature and pressure loss of different channels

Channel type	Smooth channel	Uniform channel	Non-uniform channel of case 1	Non-uniform channel of case 2
Temperature				
T_{\max}/K	1148.6	1141.5	1139.3	1139.9
T_{ave}/K	1074.4	1049.4	1049.4	1050.2
$\Delta p/\text{kPa}$	175.6	1059.0	1059.4	1053.5

improved to 82%, 80% and 78% in the uniform channel, the non-uniform channel of case 1 and the non-uniform channel of case 2, respectively. It can be concluded that the uniform and non-uniform channels where winglet pairs are denser in the inlet section behave better in a similar way to optimise the performance.

Table 3 shows the comparison that the wall temperature of the inner flame tubes and pressure loss of cold side channel of three sets of enhanced cold-side channels with the smooth channel. Here the maximum (T_{\max}) and average (T_{ave}) values are chosen to exhibit the effect of the winglet pairs on the wall temperature. T_{\max} drops about 7–8 K, and T_{ave} drops about 35 K after the winglets are attached to the wall surface. This is because of the increase in flow turbulence, and heat transfer of cold fluid and wall. The non-uniform channel of case 1 behaves the best in decreasing the T_{\max} and T_{ave} , but the increasing gap between them is not larger than 1 K. Since the uniform and non-uniform arrangements have the same number but different configurations of WVG, this kind of active cascade control of heat transfer enhancement elements is proved to be effective in improving the power output of thermoelectric generator system and safety of flame tube wall. The pressure loss in cold side channel significantly increases after installing the WVGs, and is raised five times as against channel without WVGs. The difference of pressure loss in three sets of enhanced the cold side channels is subtle. However in case 1, arranging the denser heat transfer

enhancement elements at upstream of cold side channel can minimize the wall temperature and improve the output performance of TEG system. So this kind of arrangement is proved to be more efficient and economic.

5. Conclusions

In this work, a flow-thermal-electric multiple-physical numerical model for the MGT combustor-TE device power generation system is examined. Furthermore, the active cascade control of heat transfer enhancement elements installed at the outer wall of flame tube is examined. According to the simulated results, the following conclusions are drawn:

(1) For the TEG system with 71-pair P-N junctions in each module, the voltage and internal resistance are almost unchanged because the current decreases with the increase of load resistance. The changing trend of the output power and efficiency versus load follows parabolic curves. When R_{load} is $30\ \Omega$, the maximum output power and efficiency are 0.31 W and 0.9%. The best matching load is about 1.4 times the internal resistance in this work. However, in the traditional electrical theory, the output power of the device reaches its peak value when the external load resistance of the device is equal to the internal load resistance.

(2) Under the matched load, the output power and the TE conversion efficiency of the system increase at first and then decrease with the increase of the number of

pairs of P-N junctions. For the given systems with linearly increasing TE pairs, the maximum output power and efficiency are 0.31 W and 0.9%, which are achieved at $\gamma = 0.25$. The performance of the integrated system is the best when the filling factor (γ) is 0.25 instead of larger values, or equivalently, more electricity can be produced with fewer TE materials.

(3) The average temperature difference between the hot and cold ends of the TE module is about 33 K in the smooth channel. It increases to 53.3 K, 53.2 K and 55.5 K in the uniform channel, the non-uniform channel of case 1 and the non-uniform channel of case 2, respectively. The heat transfer is greatly improved after the winglet pairs are mounted on the cold-side channel.

(4) The average thermoelectromotive force is 0.77 V in the smooth channel. It increases to 1.29 V, 1.29 V and 1.27 V in the uniform channel, the non-uniform channel of case 1 and the non-uniform channel of case 2, respectively. After the heat transfer is enhanced, the output power is almost doubled when the smooth channel is compared to other channels. Also, the TE efficiencies are improved to 82%, 80% and 78% in the uniform channel, the non-uniform channel of case 1 and the non-uniform channel of case 2, respectively. The uniform and non-uniform channels with denser winglet pairs in the inlet section behave better in a similar way to optimise the performance. The inner surface temperatures of the flame tubes are compared. The maximum temperature drops about 7–8 K and the average temperature drops about 35 K. Since the uniform and non-uniform arrangements have the same number but different configurations, the active cascade control of heat transfer enhancement elements is proved to be effective in improving the output power of thermoelectric generator system and safety of flame tube wall.

The WVGs are usually used to enhance heat transfer in the channels. In this work, the active cascade control of heat transfer enhancement element distribution by arranging denser heat transfer enhancement elements at upstream of cold-side channel is proved to be effective in improving the output power of system without much pumping power when the large temperature drop occurs along the flow direction. Further investigation combining CFD method with machine learning method will be conducted in the near future to optimize the performance.

Acknowledgment

This work is supported by the National Natural Science Foundation of China (No. 52022080 and No. 51676155).

References

- [1] Niu J., Tian Z., Zhu J., Lu Y., Implementation of a price-driven demand response in a distributed energy system with multi-energy flexibility measures. *Energy Conversion and Management*, 2020, 208: 112575.
- [2] Zhang J., Cho H.J., Mago P.J., Zhang H.G., Yang F.B., Multi-objective particle swarm optimization (MOPSO) for a distributed energy system integrated with energy storage. *Journal of Thermal Science*, 2019, 28(6): 1221–1235.
- [3] Razavi S.E., Rahimi E., Javadi M.S., Nezhad A.E., Lotfi M., Shafiekhah M., Catalao J.P.S., Impact of distributed generation on protection and voltage regulation of distribution systems: A review. *Renewable and Sustainable Energy Reviews*, 2019, 105: 157–167.
- [4] Han D.J., Hao L., Yang J.F., Experimental investigations on vibration characteristics for bearing-rotor system of micro gas turbine. *Proceedings of the 10th International Conference on Rotor Dynamics – IFToMM*, Rio de Janeiro, Brazil, 2018, pp. 343–356. DOI: 10.1007/978-3-319-99272-3_24.
- [5] Pilavachi P.A., Mini- and micro-gas turbines for combined heat and power. *Applied Thermal Engineering*, 2002, 22(18): 2003–2014.
- [6] Rodgers C., Turbochargers to small gas turbines, 1997, ASME Paper 97-GT-200.
- [7] Toshio N., Lessons learnt from the ultra-micro gas turbine development at University of Tokyo. *Micro Gas Turbines*, 2005, 14: 1–58.
- [8] McDonald C.F., Low-cost compact primary surface recuperator concept for microturbines. *Applied Thermal Engineering*, 2000, 20(5): 471–497.
- [9] Loeser M., Redfern M.A., Modelling and simulation of a novel micro-scale combined feedstock biomass generation plant for grid-independent power supply. *International Journal of Energy Research*, 2010, 34(4): 303–320.
- [10] Perna A., Minutillo M., Jannelli E., Jannelli E., Cigolotti V., Nam S.W., Yoon K.J., Performance assessment of a hybrid SOFC/MGT cogeneration power plant fed by syngas from a biomass down-draft gasifier. *Applied Energy*, 2018, 227: 80–91.
- [11] Yazawa K., Fisher T.S., Groll E.A., Shakouri A., High exergetic modified brayton cycle with thermoelectric energy conversion. *Applied Thermal Engineering*, 2017, 114: 1366–1371.
- [12] Bass J.C., Elsner N.B., Leavitt F.A., Performance of the 1 kW thermoelectric generator for diesel engines. *AIP Conference Proceedings*, 1994, 316(1): 295–298. DOI: 10.1063/1.46818.
- [13] Cuce E., Cuce P.M., Guclu T., Besir A.B., On the use of nanofluids in solar energy applications. *Journal of Thermal Science*, 2020, 29(3): 513–534.
- [14] Pan T., Gong T.R., Yang W., Wu Y.J., Numerical study on the thermal stress and its formation mechanism of a thermoelectric device. *Journal of Thermal Science*, 2018,

- 27(3): 249–258.
- [15] Zhang Y.L., Wang X.W., Cleary M., Schoensee L., Kempf N., Richardson J., High-performance nanostructured thermoelectric generators for micro combined heat and power systems. *Applied Thermal Engineering*, 2016, 96: 83–87.
 - [16] Wang J., Song X.X., Li Y.L., Zhang C.Z., Modeling and analysis of thermoelectric generators for diesel engine exhaust heat recovery system. *Journal of Energy Engineering*, 2020, 146 (2): 04020002.
 - [17] He Z.M., Foo M.X., Yong D., Ma T., Hao Y., Zhang H., Ding D., Non-imaging optics for improving waste heat collection with thermoelectrics. *ES Energy and Environment*, 2019, 6: 78–84.
 - [18] Tian H., Sun X.X., Jia Q., Liang X.Y., Shu G.Q., Wang X., Comparison and parameter optimization of a segmented thermoelectric generator by using the high temperature exhaust of a diesel engine. *Energy*, 2015, 84: 121–130.
 - [19] Meng J.H., Wang X.D., Chen W.H., Performance investigation and design optimization of a thermoelectric generator applied in automobile exhaust waste heat recovery. *Energy Conversion and Management*, 2016, 120: 71–80.
 - [20] Zhou Z.G., Zhu D.S., Wu H.X., Zhang H.S., Modeling, experimental study on the heat transfer characteristics of thermoelectric generator. *Journal of Thermal Science*, 2013, 22(1): 48–54.
 - [21] Yu J.L., Zhao H., A numerical model for thermoelectric generator with the parallel-plate heat exchanger. *Journal of Power Sources*, 2007, 172(1): 428–434.
 - [22] Niu X., Yu J.L., Wang S.Z., Experimental study on low-temperature waste heat thermoelectric generator. *Journal of Power Sources*, 2009, 188(2): 621–626.
 - [23] Ma T., Qu Z.M., Yu X.F., Lu X., Chen Y.T., Wang Q.W., Numerical study and optimization of thermoelectric-hydraulic performance of a novel thermoelectric generator integrated recuperator. *Energy*, 2019, 174: 1176–1187.
 - [24] Lu X., Yu X.F., Qu Z.M., Wang Q.W., Ma T., Experimental investigation on thermoelectric generator with non-uniform hot-side heat exchanger for waste heat recovery. *Energy Conversion and Management*, 2017, 150: 403–414.
 - [25] Qiu K., Hayden A.C.S., Development of a thermoelectric self-powered residential heating system. *Journal of Power Sources*, 2008, 180(2): 884–889.
 - [26] Alanne K., Laukkanen T., Saari K., Jokisalo J., Analysis of a wooden pellet-fueled domestic thermoelectric cogeneration system. *Applied Thermal Engineering*, 2014, 63(1): 1–10.
 - [27] Wang F.S., Kong W.J., Wang B.R., Experimental study of combustion on a micro gas turbine combustor. *Proceedings of ASME Turbo Expo 2008: Power for Land, Sea and Air*, Berlin, Germany, 2008, 3: 749–755. DOI: 10.1115/GT2008-50975.
 - [28] Angrist S.W., *Direct energy conversion*, third ed., Allyn and Bacon Inc., Boston, 1976.
 - [29] Reddy B.V.K., Barry M., Li J., Chyu M.K., Three dimensional multiphysics coupled field analysis of an integrated thermoelectric device. *Numerical Heat Transfer, Part A: Applications*, 2012, 62(12): 933–947.
 - [30] Gomez M., Reid R., Ohara B., Lee H., Influence of electrical current variance and thermal resistances on optimum working conditions and geometry for thermoelectric energy harvesting. *Journal of Applied Physics*, 2013, 113(17): 174908.
 - [31] Yu X.F., Lu X., Wang Q.W., Ma T., Parametric study of thermoelectric power generators under large temperature difference conditions. *Applied Thermal Engineering*, 2018, 144: 647–657.